

Effect of Disorder in a Three-Dimensional Layered Chern Insulator

Shang Liu,¹ Tomi Ohtsuki,² and Ryuichi Shindou^{3,4,*}

¹*School of Physics, Peking University, Beijing 100871, China*

²*Department of Physics, Sophia University, Chiyoda-ku, Tokyo, 102-8554, Japan*

³*International Center for Quantum Materials, Beijing, 100871, China*

⁴*Collaborative Innovation Center of Quantum Matter, Beijing, 100871, China*

We studied effects of disorder in a three dimensional layered Chern insulator. By calculating the localization length and density of states numerically, we found two distinct types of metallic phases between Anderson insulator and Chern insulator; one is diffusive metallic (DM) phase and the other is renormalized Weyl semimetal (WSM) phase. We show that longitudinal conductivity at the zero energy state remains finite in the renormalized WSM phase as well as in the DM phase, while goes to zero at a semimetal-metal quantum phase transition point between these two. Based on the Einstein relation combined with the self-consistent Born analysis, we give a conductivity scaling near the quantum transition point.

PACS numbers: 71.30.+h, 05.70.Jk, 71.23.-k, 71.55.Ak, 73.20.At, 73.61.-r

Introduction. — During the last decade, huge research effort has been made on topological phases in condensed matter physics [1, 2]. Among many others, the critical nature of the quantum phase transition between the topological phase and nontopological phase is one of the most fundamental research issues in the studies of topological phases. A classic example is the localization problem in the two-dimensional (2D) integer quantum Hall (QH) phase [3] (or so-called ‘Chern insulator’ [4–6]), where a bulk delocalized state is universally observed between topologically distinct integer QH phases [7–9]. The existence of the bulk delocalized state comes from the stability of topological edge modes in respective integer QH phases [10], while its ‘zero-measure’ property is compatible with the scaling theory of the Anderson localization [11]. In fact, weak interlayer couplings among 2D QH layers make the QH quantum critical point into a finite width of 3D metallic phase [12, 13].

In theoretical studies, preceding efforts demonstrated that multiple-layered Chern insulators (CI) result in a novel semimetal phase, dubbed as ‘Weyl semimetal’ [14–17], where a pair of band touching points appear in the 3D momentum space. The pair can be regarded as topological defects having opposite magnetic charges, so to speak, ‘magnetic monopole’ and ‘antimonopole’. On increasing interlayer couplings, the monopole in relative to the antimonopole winds up the 3D Brillouin zone at least once, only to annihilate with the antimonopole again. This pair creation and annihilation process changes a global topological feature encoded in electronic Bloch wavefunctions, which ‘allows’ the system to enter into another kind of topological phase or non-topological gapped phase. When comparing these Weyl semimetal (WSM) physics with localization problem in integer QH physics, one may naturally ask ‘how the 2D QH quantum critical point is connected with 3D WSM phase?’ or ‘Can we obtain a new insight to the localization physics in 2D QH system from the viewpoint of the 3D WSM physics?’

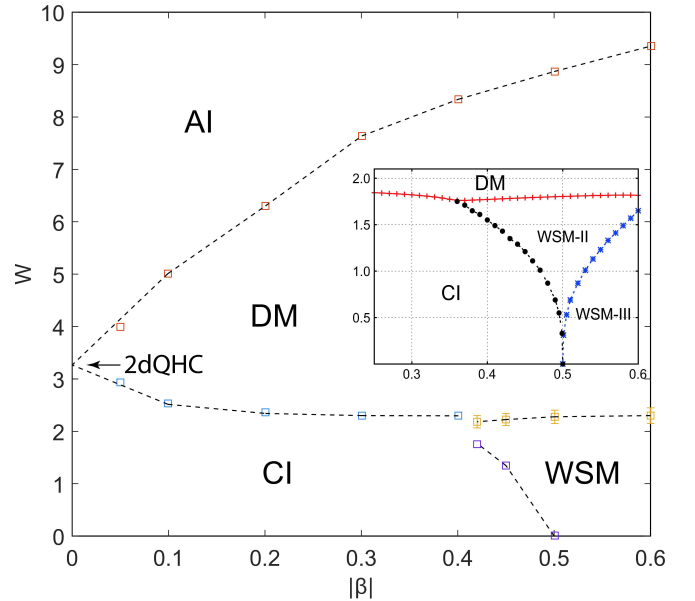


FIG. 1. (color online) Phase diagram of layered Chern insulator subtended by disorder strength W and the interlayer coupling strength $|\beta|$. WSM, DM, CI, AI and 2dQHC stand for renormalized Weyl semimetal, diffusive metal, Chern insulator, ordinary Anderson insulator and 2D QH quantum critical point, respectively. (inset) Phase diagram obtained from the self-consistent Born analysis. The region-II WSM phase (WSM-II) has two pairs of the Weyl points, while the region-III WSM phase (WSM-III) has three pairs of the Weyl points [20].

In this Letter, we will answer these questions, by studying numerically disorder effects in a layered Chern insulator. A computation of the localization length and two-terminal conductance by the transfer matrix (TM) method [18] and density of states by the kernel polynomial expansion (KPE) method [19] reveals two distinct kinds of metallic phases, which intervene between conventional Anderson insulator (AI) and layered Chern in-

sulator (CI) in a phase diagram subtended by the layer coupling and the disorder strength; one is (i) diffusive metallic (DM) phase with its zero-energy state, i.e. an electronic state at the band touching point ($E = 0$), having a finite life time and the other is (ii) renormalized WSM phase whose zero-energy state has an infinite life time while the velocity and location in the \mathbf{k} space of gapless Weyl fermions being strongly renormalized by disorder. A scaling analysis of the density of states clarifies a critical nature of the phase transition line between these two metallic phases. A finite-size-scaling of the conductance also shows that finite conductivities in DM phase and in WSM phase go to zero toward the quantum critical line.

Model.— We study a spinless two-orbital tight-binding model on a cubic lattice, which comprises of s -orbital and $p \equiv p_x + ip_y$ orbital; [5]

$$\begin{aligned} \mathcal{H} = & \sum_{\mathbf{x}} \left([\epsilon_s + v_s(\mathbf{x})] c_{\mathbf{x},s}^\dagger c_{\mathbf{x},s} + [\epsilon_p + v_p(\mathbf{x})] c_{\mathbf{x},p}^\dagger c_{\mathbf{x},p} \right) \\ & + \sum_{\mathbf{x}} \left(- \sum_{\mu=x,y} (t_s c_{\mathbf{x}+\mathbf{e}_{\mu},s}^\dagger c_{\mathbf{x},s} - t_p c_{\mathbf{x}+\mathbf{e}_{\mu},p}^\dagger c_{\mathbf{x},p}) \right) \\ & + t_{sp} \sum_{\mathbf{x}} (c_{\mathbf{x}+\mathbf{e}_x,p}^\dagger - c_{\mathbf{x}-\mathbf{e}_x,p}^\dagger) c_{\mathbf{x},s} \\ & - it_{sp} \sum_{\mathbf{x}} (c_{\mathbf{x}+\mathbf{e}_y,p}^\dagger - c_{\mathbf{x}-\mathbf{e}_y,p}^\dagger) c_{\mathbf{x},s} \\ & - (t'_s c_{\mathbf{x}+\mathbf{e}_z,s}^\dagger c_{\mathbf{x},s} + t'_p c_{\mathbf{x}+\mathbf{e}_z,p}^\dagger c_{\mathbf{x},p}) + \text{H.c.} \Big), \quad (1) \end{aligned}$$

where ϵ_s , ϵ_p and $v_s(\mathbf{x})$, $v_p(\mathbf{x})$ denote atomic energies for the s , p orbital and disorder potential for the s , p orbital, respectively. Both $v_s(\mathbf{x})$ and $v_p(\mathbf{x})$ are uniformly distributed within $[-W/2, W/2]$ with identical probability distribution. t_s , t_p and t_{sp} are intralayer transfer integrals between neighboring s orbitals, p orbitals and that between s and p orbital, respectively, while t'_s and t'_p are interlayer transfer integrals. Without interlayer coupling, the model reduces to a 2D CI, given that the so-called band inversion condition is satisfied; $0 < |\epsilon_s - \epsilon_p| < 4(t_s + t_p)$. In the rest of this Letter, we take $\epsilon_s - \epsilon_p = -2(t_s + t_p)$, while $t'_s = -t'_p > 0$ and $t_s = t_p > 0$, $t_{sp} = 4t_s/3$ with $4t_s$ being the energy unit. [20] This parameter set realizes a CI with a large band gap in the 2D limit ($\beta \equiv \frac{t'_p - t'_s}{2(t_s + t_p)} = 0$) for the half filling case. When $0 \leq |\beta| < 1/2$, the system is fully gapped, which belongs to the CI phase in the 2D limit. When $|\beta| > 1/2$, the system enters into 3D WSM phase, where three pairs of the monopoles and antimonopoles appear at $\mathbf{k} = (0, \pi, \pi \pm k_0)$, $(\pi, 0, \pi \pm k_0)$ and $(\pi, \pi, \mp k_1)$ respectively. The Weyl points at $(0, \pi, \pi - k_0)$, $(\pi, 0, \pi - k_0)$ and $(\pi, \pi, -k_1)$ are the magnetic monopoles with positive magnetic charge, while the others are the antimonopoles with negative charge. At $|\beta| = \frac{1}{2}$, three pairs of monopoles and antimonopoles annihilate with each other simultaneously, i.e. $k_0 = k_1 = 0$.

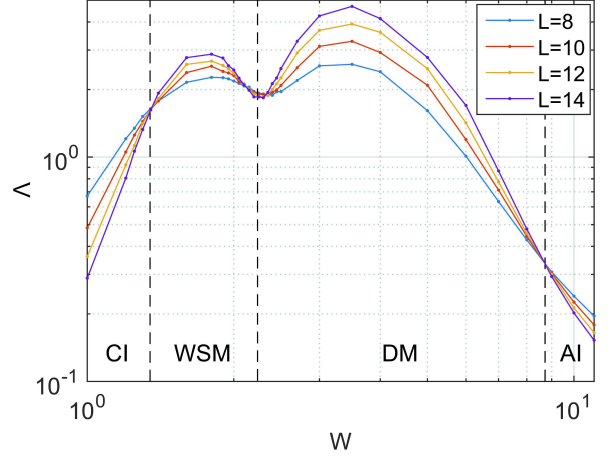


FIG. 2. (color online) Localization length normalized by the system size, Λ , as a function of disorder strength for $|\beta| = 0.45$ and various system size L . For a guide to the eyes, we put three vertical dotted lines for the scale-invariant critical points where the localization length barely changes with L . We note that the system is highly anisotropic, and the transfer matrix calculation along x -direction (in-plane direction) seems to suffer large corrections to scaling.

Localization Length and Phase Diagram.— By the TM method, the localization length along the z -direction (the stacking direction) is calculated for various system sizes ($N \equiv L^2 \times 10^5 \sim 10^6$ with $L = 8, 10, 12, 14$, L being the linear dimension of the cross section) as a function of W and $|\beta|$. In the presence of finite interlayer coupling ($|\beta| \neq 0$), the QH critical point in the 2D limit becomes a finite window of a metallic region between AI and CI. With larger coupling, the finite region of the metallic phase become two distinct metallic phases, which are separated by a critical line. One is in stronger disorder side and is connected with the 2D QH critical point, while the other is in weaker disorder side and belongs to the same phase as the 3D WSM phase in the clean limit (Fig. 1). These two metallic phases are always separated by a transition line where the localization length ξ normalized by the linear dimension of the system size L barely changes as a function of L (Fig. 2) [21–23]. The scale-invariant behaviour of $\Lambda \equiv \xi/L$ suggests existence of quantum critical line between these two metallic phases.

Density of States.— To characterize this critical line, we computed the density of states (DOS) in terms of the KPE method for several different cubic system sizes ($N = L^3$ with $L = 40, 48, 60$ and 80), to extrapolate the thermodynamic behaviour of the DOS based on $\rho_L(E, W) = \rho(E, W) + b(E, W)/L^2$ [20]. Here $\rho_L(E, W)$ denotes the DOS as a function of the electron energy E and W for the linear dimension L . The intercept $\rho(E, W)$ as a function of $1/L^2$ can be regarded as the density of states in the thermodynamic limit. Fig.3 shows the DOS

near the zero energy for those disorder strengths around the phase transition between the two metallic phases. The DOS for the weaker disorder side vanishes at the zero energy, where $\rho(E, W)$ becomes a parabolic function in E . The DOS in the stronger disorder side acquires a finite value at $E = 0$ [24–27]. This feature is consistent with self-consistent Born analyses (SCBA) [20, 25, 28, 29] and renormalization group (RG) analysis [24, 30], suggesting that the former metallic phase belongs to the same phase as the WSM phase in the clean limit; renormalized WSM phase whose zero-energy state (an electronic state at the band touching point; $E = 0$) has an infinite life time. Meanwhile the latter phase is characterized by the zero-energy state having a finite life time; diffusive metallic (DM) phase.

In the renormalized WSM phase, the density of states near $E = 0$ is determined by an effective Hamiltonian linearized near the gapless points, $H_{\mathbf{k}} = \sum_i v_i p_i \sigma_i$, where \mathbf{v} is a renormalized velocity and $\mathbf{p} \equiv \mathbf{k} - \mathbf{k}_0$ the momentum distance from the respective Weyl point \mathbf{k}_0 . Each Weyl point contributes to DOS near $E = 0$ as $\rho(E) = \frac{1}{L^3} \sum_{\mathbf{p}} \delta(E - E_{\mathbf{p}}) = \frac{1}{2\pi^2 \bar{v}^3} E^2$, with $\bar{v} \equiv |v_x v_y v_z|^{1/3}$ being an averaged velocity. On increasing the disorder strength, the renormalized velocity \bar{v} evaluated from the coefficient of E^2 decreases toward a certain critical point ($W = W_c$); purple squares in Fig. 3b. At the same point, $\rho(0)$ starts to take a finite non-negligible value; blue circles in Fig. 3b, where the SCBA identifies $\rho(0)$ as inversely proportional to the life time of the zero-energy state [20]. We also find that all the data points for the density of states near $E = 0$ collapse into a single-parameter scaling function form, $\rho(E) = \delta^{(3-z)\nu} f(|E|\delta^{-z\nu})$, with $\delta \equiv |W - W_c|/W_c$ [26, 31]. By fitting the DOS curves into this scaling function, we determine the dynamical exponent $z = 1.53 \pm 0.03$ and $\nu = 0.84 \pm 0.1$. [20] The scaling analysis in combination with the SCBA unambiguously conclude the existence of the quantum critical line between DM phase and WSM phase at $W = W_c$.

Two-Terminal Conductance and Conductivity — To characterize the renormalized WSM and DM phases, we calculated the two-terminal conductance G in the in-plane direction (x -direction) for the cubic system size with various linear dimensions (L^3 with $L = 6, 8, \dots, 30$) via the transfer matrix method [32]. In the other two spatial directions (y and z -directions), we impose either periodic boundary condition (G^p) or open boundary condition (G^o). In the Chern insulator (CI) phase, G^p is nearly zero at $L = 30$, while, for the two metallic phases, an in-plane bulk conductivity σ_b is obtained from G^p by the linear fitting ($G^p = \sigma_b L + b$).

The calculated result shows that finite conductivity in the DM and the WSM phase reduces to zero toward $W = W_c$ (Fig. 4). When combined with the SCBA result, this behaviour is consistent with the Einstein relation for the

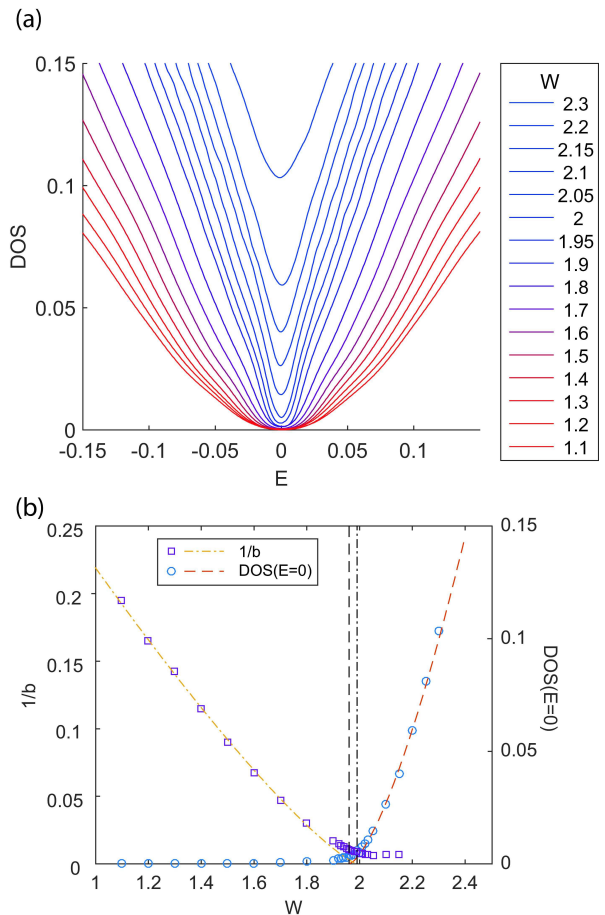


FIG. 3. (color online) (a) Density of states (DOS) at $|\beta| = 0.6$ near the zero energy state for those W near the critical point intervening between DM and WSM phase. W increases from bottom to top. (b) Zero-energy density of states $\rho(E = 0)$ and cube of averaged velocity \bar{v} as a function of W . The latter is evaluated from the fitting of $\rho(E)$ to $a + bE^2$ with $\bar{v}^3 \propto 1/b$ and free parameter a (see also text). The vertical dot-dashed line and dashed line denote the critical disorder strength at which \bar{v} and $\rho(E = 0)$ vanish, respectively (see Ref. 20 for their determinations).

conductivity $\sigma(E)$;

$$\sigma(E) = e^2 D(E) \rho(E). \quad (2)$$

The diffusion constant $D(E)$ is given by the life time τ and the averaged velocity \bar{v} as $D(E) = \frac{\bar{v}^2 \tau}{3}$. SCBA relates $\rho(E)$ with the inverse of the life time as $\rho(E) = 24/(\pi \tau W^2)$ [20]. Thus the relation tells that $\sigma(E = 0) = 8e^2 \bar{v}^2 / (\pi W^2)$ remains finite not only in the DM phase but also in the renormalized WSM phase. Moreover, since \bar{v} vanishes at the critical point as above [26], the Einstein relation also dictates that the conductivity reduces to zero at the critical point, being consistent with our numerical observation (blue points near $W = 2$ in Fig. 4). Note also that $\sigma(E = 0)$ vanishes as $\delta^{(d-2)\nu}$ from the DM side while \bar{v} vanishes as $\delta^{(z-1)\nu}$ from the WSM side [26].

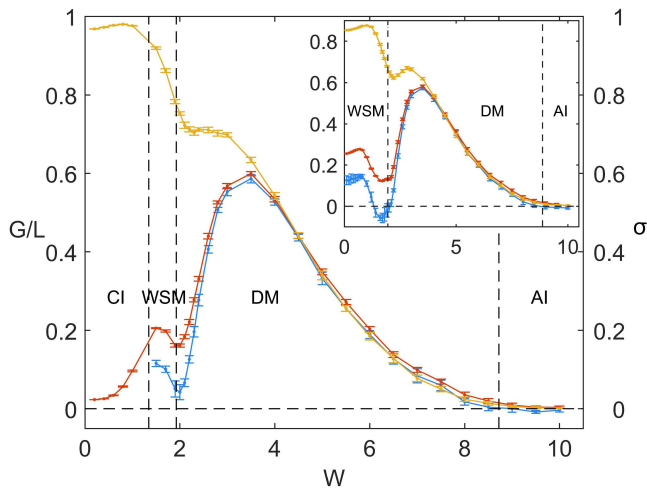


FIG. 4. (color online) Bulk conductivity and conductances of the cubic system (L^3) at $|\beta| = 0.45$ (inset: at $|\beta| = 0.50$) as a function of disorder strength W ; the bulk conductivity σ_b (blue points with line), conductance with the periodic boundary condition G^p ($L = 30$; red points with line) and that with open boundary condition G^o ($L = 30$; yellow points with line). The vertical dotted lines around $W = 1.92$ ($|\beta| = 0.45$) and $W = 1.96$ ($|\beta| = 0.50$) stand for the WSM-DM transition points determined by the DOS, while the vertical dotted lines around $W = 8.7$ ($|\beta| = 0.45$) and $W = 8.9$ ($|\beta| = 0.50$) and that around $W = 1.35$ ($|\beta| = 0.45$) are the DM-AI transition points and CI-WSM transition point determined from the localization length, respectively.

With our expression for the conductivity $\sigma(E = 0) \propto \bar{v}^2$, we see that the conductivity vanishes continuously from the WSM side as $\sigma(E = 0) \propto \delta^{2(z-1)\nu}$. This is qualitatively consistent with Ref. 33, which predicts a continuously vanishing conductivity with a different exponent $\sigma(E = 0) \propto \delta$. If we assume that $z = d/2$, our exponent in the WSM side coincides with that from the DM side.

G^o and G^p significantly differ from each other in the Chern insulator phase and the renormalized WSM phase (Fig. 4). The difference can be attributed to the surface conductance due to the chiral surface states. In the renormalized WSM phase, the zero-energy state has an infinite life time τ , so that the SCBA is fully justified; neglected Feynman diagrams in the approximation are smaller than those included at least by a factor $1/\tau$. The SCBA result shows that the Green's function after quenched impurity averaging has either three or two pairs of Weyl points in the momentum space (inset of Fig. 1). In the region-II WSM phase, two pairs of Weyl points appear at $\mathbf{k} = (0, \pi, \pi \pm \bar{k}_0)$ and $(\pi, 0, \pi \pm \bar{k}_0)$, while another one pair appears at $(\pi, \pi, \mp \bar{k}_1)$ in the region-III WSM phase. These Weyl points in the bulk electronic state result in a surface chiral Fermi arc state with left-moving chirality connecting from the surface crystal momentum $(k_x, k_z) = (0, \pi - \bar{k}_0)$ to $(0, -\pi + \bar{k}_0)$, and two other chiral arc states with right-moving chirality, one connecting

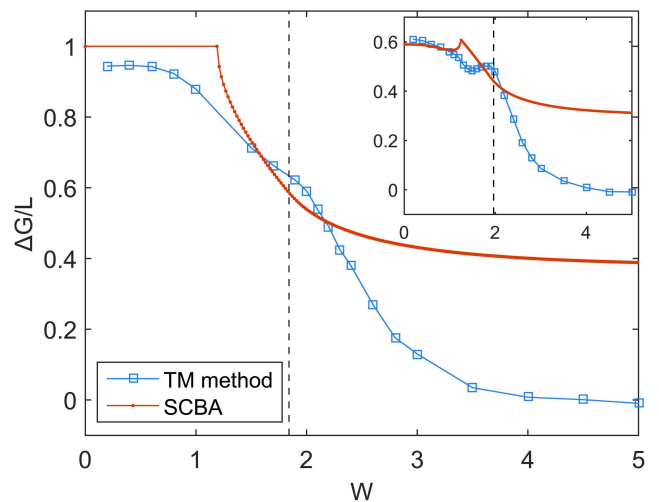


FIG. 5. (color online) $\Delta G \equiv G^o - G^p$ for $|\beta| = 0.45$ (inset for $|\beta| = 0.55$), where G^o and G^p are calculated for the cubic system ($L^3 = 30^3$). The red solid line is a surface conductance evaluated from eq. (3) along with the SCBA result for the same parameter set.

from $(\pi, \pi - \bar{k}_0)$ to (π, \bar{k}_1) and the other from $(\pi, -\bar{k}_1)$ to $(\pi, -\pi + \bar{k}_0)$. They in total lead to a finite two-terminal surface conductance which depends on the length of each Fermi arc. The left-moving chiral arc and right-moving arc cancel each other by the intra-surface backward scattering due to impurities, so that the surface conductance is expected to be expressed with the difference between the length of right-moving arc ($2\pi - 2\bar{k}_0 - 2\bar{k}_1$) and that of the left-moving arc ($2\bar{k}_0$);

$$\Delta G \equiv G^o - G^p = \frac{e^2}{h} \frac{(\pi - 2\bar{k}_0 - \bar{k}_1)L}{\pi}. \quad (3)$$

In fact, \bar{k}_0 and \bar{k}_1 obtained from the SCBA along with eq. (3) reproduces ΔG from the numerics at the quantitative level for $W < W_c$ (Fig. 5). Importantly, paired two Weyl nodes do *not* annihilate with each other even at $W = W_c$; the associated chiral surface Fermi arc state *does* survive up to $W = W_c$. For $W > W_c$, each Weyl node acquires a finite line broadening (inverse of lifetime), so that the chiral Fermi arc states near the two ends of the arc start to be mixed with bulk states and lose their protected surface conduction property. Meanwhile, those arc states away from the two ends still contribute to robust surface conduction for $W \gtrsim W_c$. [20] This picture is consistent with our numerical observation of the finite surface conductance ΔG for $W \gtrsim W_c$, which is smaller than the SCBA estimate from Eq. (3) in the DM phase.

Conclusion— In this Letter, we introduce a simple lattice model in the unitary class, which enables us to study WSM phase, disorder-induced DM phase and quantum phase transition between these two phases. The critical nature of the phase transition is confirmed by the

scale-invariant behaviour of the localization length and by the scaling analysis of the density of states. The calculated critical exponents take those values close to critical exponents previously obtained in a lattice model of the symplectic class [26]. We show that longitudinal conductivity at the zero-energy state remains finite in the renormalized WSM phase as well as in the DM phase, while it reduces to zero toward the transition point. With the help of the SCBA, we show that this observation is consistent with the Einstein relation for the conductivity and Wegner's conductivity scaling [34]. The two-terminal conductance shows a significant residual surface conductance at the transition point, which can be attributed to the "renormalized" chiral Fermi arc states.

Acknowledge The authors would like to thank Dr. Koji Kobayashi for fruitful discussions. This work was supported by JSPS KAKENHI Grants No.15H03700 and No. 24000013 and by NBRP of China (Grant No. 2015CB921104).

Note added. – Recently we became aware of independent numerical works [35] that treat similar situation but focus on a different aspect.

SUPPLEMENTAL MATERIALS

Weyl semimetal phases and chiral Fermi arc in layered Chern insulator

The tight-binding Hamiltonian for layered Chern insulator [4, 5] reduces to the following 2×2 Hamiltonian in the momentum space,

$$\mathbf{H}(\mathbf{k}) = a_0 \sigma_0 + \mathbf{a} \cdot \boldsymbol{\sigma} \quad (4)$$

with $\boldsymbol{\sigma} = (\sigma_x, \sigma_y, \sigma_z)$ are Pauli matrices and

$$a_0(\mathbf{k}) = \frac{\epsilon_s + \epsilon_p}{2} + (t_p - t_s)(\cos k_x + \cos k_y) - (t'_s + t'_p) \cos k_z$$

$$a_3(\mathbf{k}) = \frac{\epsilon_s - \epsilon_p}{2} - (t_p + t_s)(\cos k_x + \cos k_y) - (t'_s - t'_p) \cos k_z$$

$$a_1(\mathbf{k}) = -2t_{sp} \sin k_y,$$

$$a_2(\mathbf{k}) = -2t_{sp} \sin k_x,$$

respectively. For simplicity, we take $t_p = t_s > 0$ and $t'_s = -t'_p$ so that the \mathbf{k} -dependence of a_0 can be omitted and the direct band gap always becomes the global band gap $\Delta(\mathbf{k}) = 2 \min |\mathbf{a}(\mathbf{k})|$. If any, the gap closing occurs at the high symmetric \mathbf{k} lines, i.e. $\mathbf{k} = (0, 0, k_z), (\pi, 0, k_z), (0, \pi, k_z), (\pi, \pi, k_z)$. At these points, the gap is given as a function of k_z

$$\Delta(\mathbf{k}) = 2(t_s + t_p) \cdot \left| \alpha - \frac{\cos k_x + \cos k_y}{2} + \beta \cos k_z \right|,$$

with $\alpha \equiv \frac{\epsilon_s - \epsilon_p}{4(t_s + t_p)}$ and $\beta \equiv \frac{t'_p - t'_s}{2(t_s + t_p)} = -\frac{t'_s}{2t_s}$. This gives a phase diagram subtended by α and β depicted

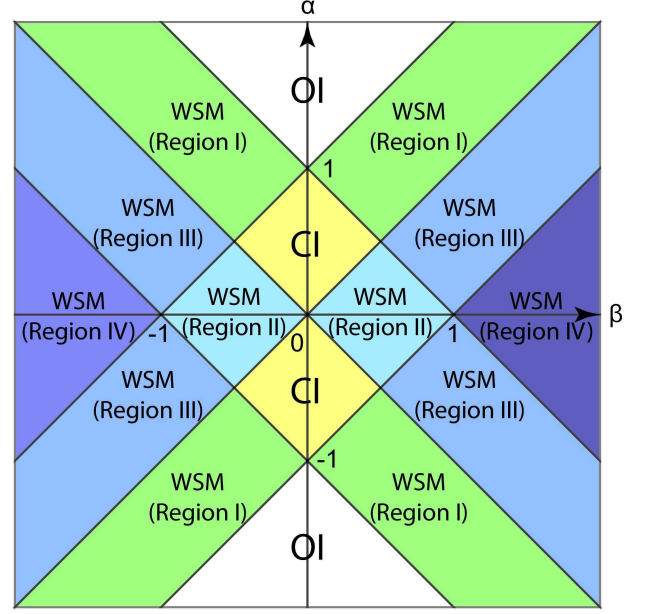


FIG. 6. (color online) Phase diagram of layered Chern insulator in the clean limit. OI and CI denote ordinary band insulator and Chern insulator respectively, while WSM denotes the Weyl semimetallic phases. The explanation for four distinct regions of the WSM phase is given in the text of this supplemental material.

in Fig. 6. The phase diagram comprises of Chern insulator phases and conventional band insulator phases, and four Weyl semimetal phases; WSM in the region I has one pair of two Weyl points having opposite magnetic charges (either at $\mathbf{k} = (0, 0, \pm*)$ or $(\pi, \pi, \pm*)$), WSM in the regions II has two pairs (at $\mathbf{k} = (\pi, 0, \pm*), (0, \pi, \pm*)$). In the region III and VI, it has three pairs (either at $\mathbf{k} = (0, 0, \pm*), (\pi, 0, \pm*), (0, \pi, \pm*),$ or at $(\pi, \pi, \pm*), (\pi, 0, \pm*), (0, \pi, \pm*)$) and four pairs respectively. In the main text, we took $\alpha = -\frac{1}{2}$, so that, on increasing $|\beta|$, the system enters the region III first ($\frac{1}{2} < |\beta| < \frac{3}{2}$) and then region IV ($\frac{3}{2} < |\beta|$). Figure 7 shows surface chiral Fermi arcs in the case of $|\beta| = 0.6$, where the right-moving chiral Fermi arc connects from a surface momentum point $(k_x, k_z) = (0, \pi - k_0)$ to $(0, -\pi + k_0)$ with $k_0 \equiv \cos^{-1}[\frac{\alpha}{\beta}]$, while the two left-moving chiral Fermi arcs connect from $(k_x, k_z) = (\pi, k_1)$ to $(\pi, \pi - k_0)$ and from $(k_x, k_z) = (\pi, -k_1)$ to $(\pi, -\pi + k_0)$ respectively with $k_1 \equiv \cos^{-1}[-\frac{1+\alpha}{\beta}]$.

Self-consistent Born analysis

A single-point Green function is averaged over the on-site impurity potentials,

$$[\mathbf{G}_{\pm}(\mathbf{k}, \mathbf{k}')]_{\alpha, \beta} \equiv \langle \langle \mathbf{k}, \alpha | \frac{1}{E - \mathcal{H}_0 - \mathcal{V} \pm i\delta} | \mathbf{k}', \beta \rangle \rangle_{\text{imp}} \quad (5)$$

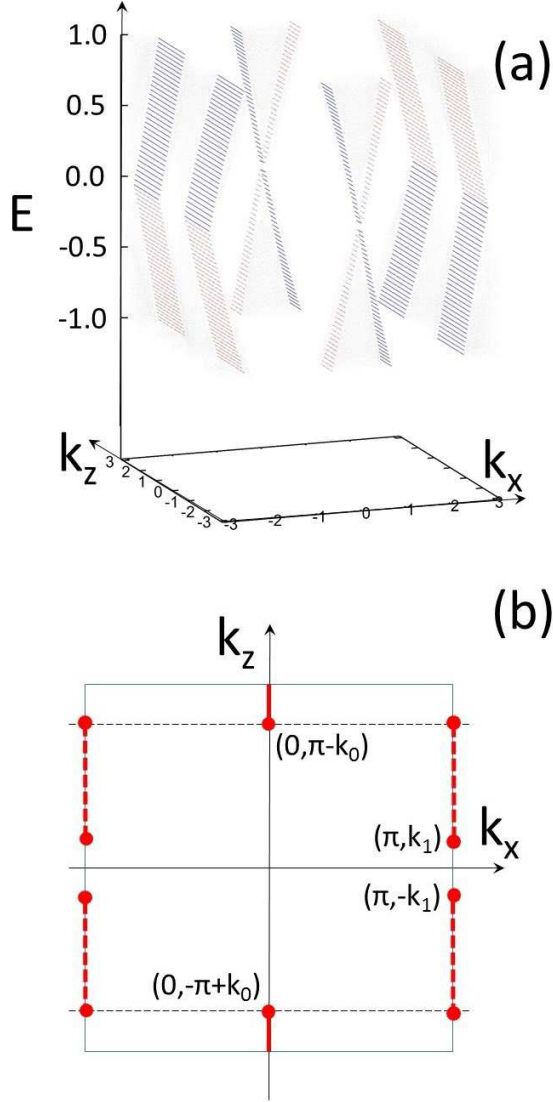


FIG. 7. (color online) (a) Energy dispersion of chiral Fermi surface states localized at one surface (red) and at the other (blue). Those energy states with grey color points are bulk states. (b) Location of chiral Fermi arcs are depicted on the surface crystal momentum space (the k_x - k_z plane), where a red solid line stands for a right-moving chiral Fermi surface state ($dE/dk_x > 0$), and red dotted lines are for left-moving chiral Fermi surface states ($dE/dk_x < 0$).

where $|\mathbf{k}, \alpha\rangle \equiv |\mathbf{k}\rangle|\alpha\rangle$, $|\mathbf{k}\rangle$ a plane-wave state with momentum \mathbf{k} , and $|\alpha\rangle$ either s or p orbital. \mathcal{H}_0 is the non-interacting Hamiltonian in the clean limit and \mathcal{V} denotes the impurity potential part in Eq. (1) in the main text, i.e. $\mathcal{V} = \sum_{\mathbf{x}} v_s(\mathbf{x})c_{\mathbf{x},s}^\dagger c_{\mathbf{x},s} + \sum_{\mathbf{x}} v_p(\mathbf{x})c_{\mathbf{x},p}^\dagger c_{\mathbf{x},p}$. The im-

purity averages are taken as follows,

$$\begin{aligned} \langle v_s(\mathbf{x}_j)v_s(\mathbf{x}_m) \rangle_{\text{imp}} &= \langle v_p(\mathbf{x}_j)v_p(\mathbf{x}_m) \rangle_{\text{imp}} \\ &= \delta_{j,m} \left(\int_{-\frac{W}{2}}^{\frac{W}{2}} v^2 dv \right) / \left(\int_{-\frac{W}{2}}^{\frac{W}{2}} dv \right) = \delta_{j,m} \frac{W^2}{12} \equiv \delta_{j,m} K. \end{aligned}$$

with $\langle v_p(\mathbf{x}_j)v_s(\mathbf{x}_m) \rangle_{\text{imp}} = 0$. Within the self-consistent Born approximation, the Green function after quenched average takes a form of $[\mathbf{G}_{\pm}(\mathbf{k}, \mathbf{k}')]_{\alpha,\beta} = \delta_{\mathbf{k},\mathbf{k}'}[\mathbf{G}_{\pm}(\mathbf{k})]_{\alpha,\beta}$ where the 2 by 2 matrix $\mathbf{G}_{\pm}(\mathbf{k})$ is given by itself,

$$\mathbf{G}_{\pm}^{-1}(\mathbf{k}) = \mathbf{G}_{0,\pm}^{-1}(\mathbf{k}) - \frac{K}{2} \frac{1}{N} \sum_{\mathbf{q}} \sum_{\mu=0,3} \sigma_{\mu} \mathbf{G}_{\pm}(\mathbf{q}) \sigma_{\mu}$$

with N the number of sites. $\mathbf{G}_{0,\pm}^{-1}(\mathbf{k})$ denotes a non-interacting Green function, $\mathbf{G}_{0,\pm}^{-1}(\mathbf{k}) \equiv (\omega \pm i\delta) - \mathbf{H}(\mathbf{k})$ with Eq. (4). The approximation takes into account all the ‘non-crossing’ diagrams, while ‘crossing’ diagrams (Feynman diagrams containing crossings of two impurity potential lines) are smaller than non-crossing diagrams by an additional factor proportional to τ^{-1} . Thus, the approximation is justified in the limit of long life-time quasiparticle ($\tau^{-1} \rightarrow 0$), which is indeed the case with the zero-energy state ($E = 0$) in the renormalized Weyl semimetal (WSM) phase (see below).

The averaged Green function is expanded in terms of the Pauli matrices with complex-valued coefficients,

$$\mathbf{G}_{\pm}^{-1}(\mathbf{k}) = b_0 \sigma_0 - \sum_{j=1}^3 b_j(\mathbf{k}) \sigma_j. \quad (6)$$

The symmetric treatment of the impurity average ($\langle v_s v_s \rangle_{\text{imp}} = \langle v_p v_p \rangle_{\text{imp}}$ and $\langle v_s v_p \rangle_{\text{imp}} = 0$) enables $b_1(\mathbf{k}) = a_1(\mathbf{k})$ and $b_2(\mathbf{k}) = a_2(\mathbf{k})$. $b_0 = E + i\delta - \gamma_0$ and $b_3(\mathbf{k}) = a_3(\mathbf{k}) + \gamma_3$ with \mathbf{k} -independent complex-valued coefficients γ_0 and γ_3 . These two are determined by the following coupled self-consistent equations;

$$\gamma_0 = \frac{K}{N} \sum_{\mathbf{k}} \frac{\gamma_0 - E_+}{a_1^2(\mathbf{k}) + a_2^2(\mathbf{k}) + (a_3(\mathbf{k}) + \gamma_3)^2 - (E_+ - \gamma_0)^2}, \quad (7)$$

$$\gamma_3 = -\frac{K}{N} \sum_{\mathbf{k}} \frac{a_3(\mathbf{k}) + \gamma_3}{a_1^2(\mathbf{k}) + a_2^2(\mathbf{k}) + (a_3(\mathbf{k}) + \gamma_3)^2 - (E_+ - \gamma_0)^2}. \quad (8)$$

with $E_+ = E + i\delta$

For the zero-energy state ($E = 0$), Eqs. (7) and (8) reduce to a simpler set of coupled equations. The simpler set of equations are only for $\text{Im}\gamma_0 = \tau^{-1}$ and $\text{Re}\gamma_3 \equiv M_3$ while $\text{Re}\gamma_0 = 0$ and $\text{Im}\gamma_3 = 0$;

$$\frac{1}{\tau} = \frac{1}{\tau} \frac{K}{N} \sum_{\mathbf{k}} \frac{1}{\overline{E}^2(\mathbf{k}) + \tau^{-2}}, \quad (9)$$

$$M_3 = -\frac{K}{N} \sum_{\mathbf{k}} \frac{a_3(\mathbf{k}) + M_3}{\overline{E}^2(\mathbf{k}) + \tau^{-2}}, \quad (10)$$

$$\overline{E}^2(\mathbf{k}) = a_1^2(\mathbf{k}) + a_2^2(\mathbf{k}) + (a_3(\mathbf{k}) + M_3)^2. \quad (11)$$

For weaker disorder case, the first equation can be satisfied only by putting $\tau^{-1} = 0$. The solution with $\tau^{-1} = 0$ (zero-energy state with infinite life time) corresponds to either the renormalized Weyl semimetal (WSM) phase or gapped Chern insulator (CI) phase. A critical disorder strength K_c above which the coupled equations can have a solution with finite life time ($\tau^{-1} \neq 0$) is determined by the following gap equation [25, 28],

$$1 = \frac{K_c}{N} \sum_{\mathbf{k}} \frac{1}{\bar{E}^2(\mathbf{k})} \quad (12)$$

where M_3 in $\bar{E}(\mathbf{k})$ in the right hand side is obtained from Eq. (10) with $\tau^{-1} = 0$. In fact, for $K > K_c$, finite τ can satisfy

$$1 = \frac{K}{N} \sum_{\mathbf{k}} \frac{1}{\bar{E}^2(\mathbf{k}) + \tau^{-2}}. \quad (13)$$

The finite- τ solution (zero-energy state with finite life time) corresponds to the diffusive metallic (DM) phase [25, 28].

For $K < K_c$, we solve Eq. (10) with $\tau^{-1} = 0$ in favor for M_3 (renormalized WSM or CI phases). For $K \geq K_c$, we solve Eqs. (10) and (13) for M_3 and τ (DM phase). In either cases, an electronic dispersion is renormalized by the disorder-induced mass term M_3 . In the present set of parameters with $\alpha = -\frac{1}{2}$, M_3 becomes positive. Fig. 6 suggests that the positive mass term with $\alpha = -\frac{1}{2}$ drives the CI phase and the region-III WSM phase (with three pairs of Weyl points) near $|\beta| = 0.5$ into the region-II WSM phase (with two pairs of Weyl points). Namely, for the CI phase ($\beta > -\frac{1}{2} = \alpha$), larger positive mass M_3 realizes $\alpha + M_3 > \beta$, where two pairs of Weyl points are created at $\mathbf{k} = (\pi, 0, \pi \pm \bar{k}_0)$ and $(0, \pi, \pi \pm \bar{k}_0)$ with

$$\bar{k}_0 \equiv \cos^{-1}\left[\frac{\alpha + M_3}{\beta}\right]. \quad (14)$$

For the region-III WSM phase ($\beta < -\frac{1}{2} = -1 - \alpha$), a positive mass term can satisfy $1 + \alpha + M_3 \geq -\beta$, so that a pair of two Weyl points at $\mathbf{k} = (\pi, \pi, \pm \bar{k}_1)$ annihilate with each other with

$$\bar{k}_1 \equiv \cos^{-1}\left[-\frac{1 + \alpha + M_3}{\beta}\right]. \quad (15)$$

By solving Eq. (12), we determine a phase boundary between diffusive metallic phase and renormalized WSM phases. By solving Eq. (10) with $\tau^{-1} = 0$ in favor for M_3 , we determine a boundary between the region-II WSM phase and Chern insulator from $\alpha + M_3 = \beta$, and a boundary between the region-II WSM and region-III WSM phases from $1 + \alpha + M_3 = -\beta$. This completes a phase diagram obtained from the self-consistent Born analysis (inset of Fig. 1 in the main text). By solving Eqs. (9) and (10) for M_3 and τ , we also obtain Eqs. (14) and (15); “renormalized” locations of the Weyl points in the momentum space. By substituting \bar{k}_0 and \bar{k}_1

into Eq. (3) in the main text, we calculate the surface conductance due to the “renormalized” chiral Fermi arc, $\Delta G \equiv G_o - G_p$, as a function of the disorder strength (Fig. 5 in the main text). For $K \leq K_c$, ΔG thus obtained quantitatively reproduces the numerics.

Importantly, the SCB analysis shows that paired two Weyl nodes do *not* annihilate with each other at the semimetal-metal quantum phase transition point ($K = K_c$). Thereby, the associated chiral surface Fermi arc state also *does* survive at the transition point. Instead of annihilating with each other, the two nodes acquire a finite line broadening *individually*; an inverse of their life time (τ^{-1}) evolves continuously from zero to a finite value for $K \geq K_c$ (as described above). Due to this line broadening of the Weyl nodes, those chiral surface states *near* the two ends of the arc start being mixed with bulk states, losing their protected surface conduction nature. On the one hand, those chiral surface states *far away from* the two ends still remain intact for $K \gtrsim K_c$, because they are well separated from bulk states (Fig. 8). The line broadening of the Weyl nodes evolve continuously, so that the latter surface states can still contribute to a residual surface conduction ΔG for those K *moderately* greater than K_c . In fact, the numerics (Fig. 5 in the main text) shows that a surface conductance remains finite for $W \lesssim 2W_c$, while the DM phase itself ranges up to a much larger disorder strength.

Note also that the persistence of paired two Weyl nodes at $K = K_c$ is consistent with the vanishing effective velocity \bar{v} at the transition point (observed by the density of states analysis). The SCB analysis explains $\bar{v} = 0$ at $K = K_c$ by an anomalous scaling of a renormalized chemical potential. Specifically, the SCB analysis shows that, for smaller E , the real part of b_0 in Eq. (6) is scaled with E for $K < K_c$ and with \sqrt{E} for $K = K_c$.

Within the self-consistent Born approximation, the density of states is proportional to an inverse of the life time τ ,

$$\begin{aligned} \rho(E) &\equiv -\frac{1}{\pi} \frac{1}{N} \left\langle \text{Im Tr} \left[\frac{1}{E - \mathcal{H}_0 - \mathcal{V} + i\delta} \right] \right\rangle_{\text{imp}} \\ &= -\frac{1}{\pi} \frac{1}{N} \sum_{\mathbf{k}} \text{Im tr} G_+(E, \mathbf{k}) = \frac{2}{\pi \tau K}. \end{aligned} \quad (16)$$

Numerical solutions of Eqs. (7) and (8) dictate that τ^{-1} for smaller E is proportional to E^2 in the renormalized WSM phases ($K < K_c$) [25, 28], while being scaled to \sqrt{E} at the quantum critical point ($K = K_c$). The solutions also find that the inverse of the life time of the zero-energy state in the DM phase ($K > K_c$) grows linearly in $K - K_c$ [25, 28]. $\tau^{-1} \propto E^2$ for $K < K_c$ is consistent with the behaviour of $\rho(E)$ for $W < W_c$ obtained from the kernel polynomial expansion (Fig. 3 in main text). $\tau^{-1} \propto \sqrt{E}$ at $K = K_c$ results in a dynamical exponent $z_{\text{scb}} = 2$, which is different from the exponent evaluated from the numerics ($z \simeq 1.5$). $\tau^{-1} \propto K - K_c$ at $E = 0$ for $K > K_c$

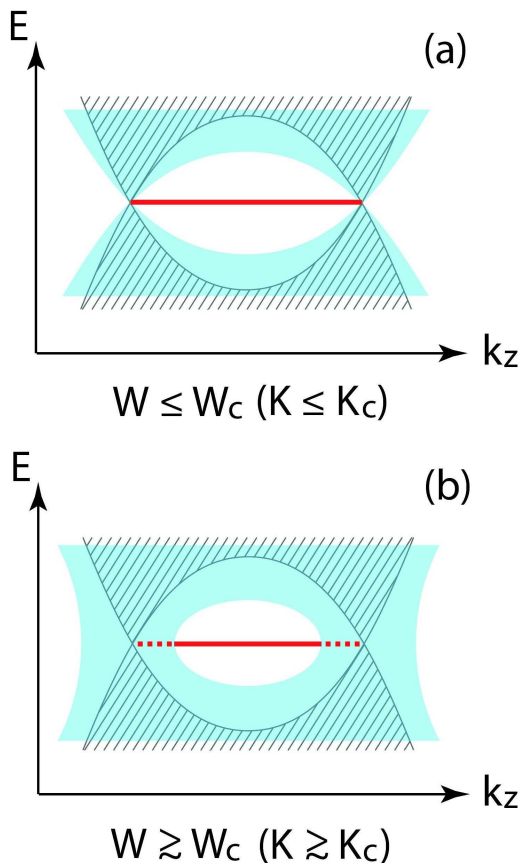


FIG. 8. (color online) Schematic pictures of an energy-momentum (surface crystal momenta) dispersion for bulk states with a pair of two Weyl nodes (black) and for corresponding chiral surface Fermi arc state at $E = 0$ (a red line). (a) $K \leq K_c$ and (b) $K \gtrsim K_c$. As in Fig. 7, the surface crystal momenta comprise of two momenta, k_x and k_z , while k_x is omitted for simplicity; the surface Fermi arc state has a chiral dispersion along the k_z direction. Note also that we only show one pair of two Weyl nodes for clarity. The disorder endows bulk states with a finite life time (line broadening), whose effect is represented by a green hatch in the figure. Within the green hatch, the crystal momentum is not well-defined even after quenched averaging of disorder potentials; any two states within the hatch are mixed with each other and indistinguishable due to the disorder. (a) for $K \leq K_c$, an inverse of the life time (line broadening) for the two Weyl nodes is zero, so that *all* the chiral arc states at $E = 0$ connecting these two nodes provide protected surface conductions. (b) for $K \gtrsim K_c$, those chiral fermi arc states at $E = 0$ which are close to the two ends of the arc (those red dotted lines covered by the green hatch) are mixed with bulk states due to the finite line broadening of the two Weyl nodes; they will not contribute to surface conductions. Meanwhile, those arc states at $E = 0$ which are well separated from the two ends (red solid line not covered by the green hatch) are *not* mixed with bulk states, providing protected surface conductions.

in combination with the dynamical exponent $z_{\text{scb}} = 2$ gives the other exponent $\nu_{\text{scb}} = 1$. Discrepancies of the critical exponents obtained from these two calculations stem from the neglected Feynman diagrams (‘crossing’ diagrams) in the self-consistent Born approximation.

The Einstein’s relation relates the longitudinal electric conductivity $\sigma(E)$ with the diffusion constant $D(E)$ and the density of states $\rho(E)$,

$$\sigma(E) = e^2 D(E) \rho(E). \quad (17)$$

The diffusion constant $D(E)$ is given by mean-free length $l = \bar{v}\tau$ and life time (mean free time) τ as $D(E) = l^2/3\tau = \bar{v}^2\tau/3$, where \bar{v} stands for an effective velocity of electrons. As shown above, the density of states $\rho(E)$ is inversely proportional to the life time within the self-consistent Born approximation. Thus, when the energy is set to the zero in the renormalized WSM phase, $\rho(E)$ vanishes as $1/\tau$, $D(E)$ diverges as τ , and the conductivity remains constant; $\sigma(E = 0) = 2\bar{v}^2/(3\pi K)$. This dictates that the conductivity at $E = 0$ remains finite not only in the diffusive metallic phase but also in the renormalized WSM phase, while vanishing at the quantum critical point intervening these two phases where $\bar{v} \rightarrow 0$ (see the main text).

Chiral surface states in layered Chern insulator and in renormalized Weyl semimetal phase

Eigenstates of Eq. (1) in the main text for a given disorder realization are numerically calculated with the periodic boundary condition along the chiral (x) and the stacking (z) directions, and open boundary condition for the other directions (y). System size $L = 80$, and numerical calculation has been done by sparse matrix diagonalization algorithm of Intel MKL/FEAST. Figure 9 shows spatial density distributions of an eigenstate ν ,

$$\rho_\nu(x, y, z) = |\psi_{\nu,s}(x, y, z)|^2 + |\psi_{\nu,p}(x, y, z)|^2.$$

We took the states ν which are closest to the zero energy ($E = 0$) in the layered Chern insulator phase region (a) ($|\beta| = 0.45$ and $W = 0.8$), and in the renormalized Weyl semimetal phase region (b) ($|\beta| = 0.45$ and $W = 1.7$). In both cases, the eigenstates are nearly localized at the boundaries ($y = \pm L/2$), suggesting that zero-energy state or eigenstates close to the zero energy are usually chiral surface states. Figure 9 also indicates that the chiral surface state in the renormalized WSM phase is spatially extended within surfaces, while the chiral state in the layered CI phase is extended only along the chiral direction and localized along the stacking direction.

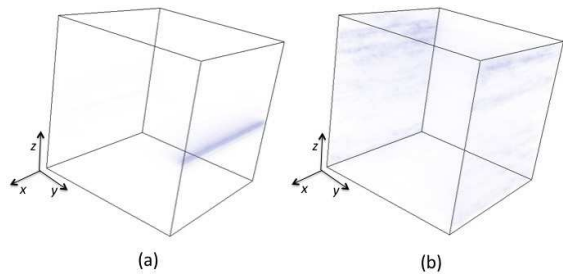


FIG. 9. (color online) Wave function density examples for layered Chern insulator (a) ($\beta = 0.45, W = 0.8, E_\nu = -0.00000859 \dots$), and a wave function density for Weyl semimetal (b) ($\beta = 0.45, W = 1.7, E_\nu = -0.0000688 \dots$). In the former case, the charge density appears one dimensionally along x direction on the $x - z$ plane, while in the latter case, the charge density appears two dimensionally on the $x - z$ plane.

Finite size scaling of the density of states

The density of states (DOS) is calculated for different system sizes ($L = 40, 48, 60, 80$) in terms of the kernel polynomial expansion method [19]. The calculated DOS is fitted with the finite size scaling form, $\rho_L(E, W) = a(E, W) + b(E, W)/L^2$ [26], which gives the DOS in the thermodynamic limit as the intercept $a(E, W)$. An example of the fitting is shown in Fig. 10 (for $\beta = -0.6, E = 0.0$ and $W = 1.5 < W_c$). The error bar obtained from this finite-size-scaling fit is shown in Fig. 11 for typical values of E and W with $\beta = -0.6$. The error is estimated with 95% confidence (2σ). Since the fitting has only two degrees of freedom, the estimated error bar is relatively large.

Parabolic fitting and the velocity

In the renormalized WSM phase ($W < W_c$), the averaged velocity of the Weyl point is obtained from a fitting of the DOS near $E = 0$ by a parabolic function $\rho(E) = a + bE^2$. Fig. 12 shows an example of the fitting ($\beta = -0.6, W = 1.5 < W_c$). On increasing $|E|$, the DOS curve changes from the E -square behavior to a E -linear behaviour. When W becomes closer to W_c from below, the E -square region becomes narrower in energy, indicating the reduction of the velocity. To estimate the curvature only around $E = 0$ from the fitting, we first observe this crossover by eye and then introduce a cut-off for $\rho(E)$ to exclude those data points in the E -linear region (For example, $\rho(E) < 0.013$ in Fig. 12).

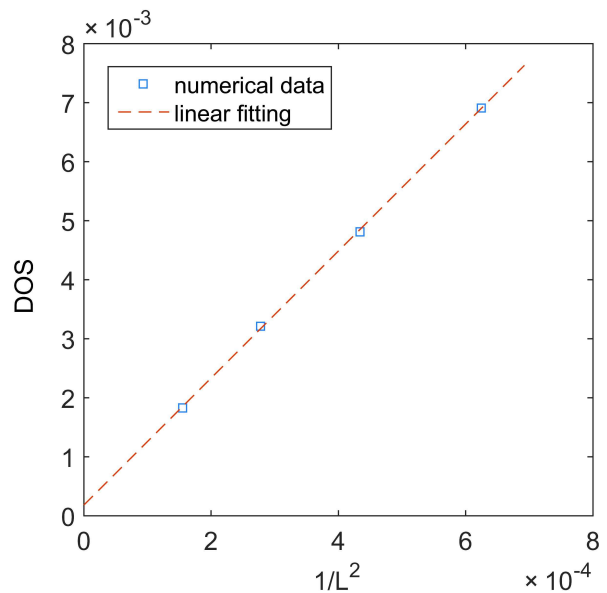


FIG. 10. (color online) Finite size scaling of the DOS at $E = 0$ and $W = 1.5$. The blue squares denote numerical data of the DOS for four different system sizes, and the red dashed line is the linear fit to $1/L^2$.

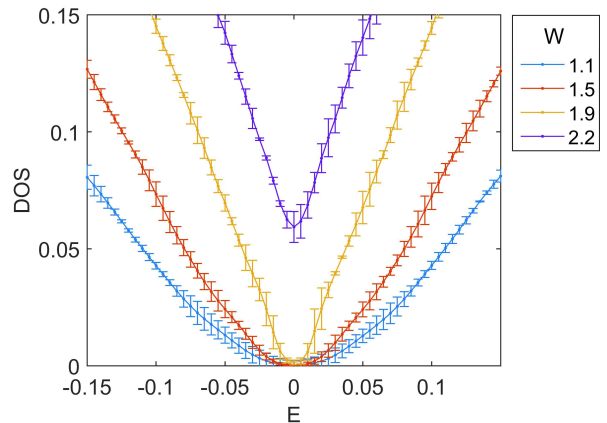


FIG. 11. (color online) The DOS from the finite size scaling for typical values of E and W . The 95% confidence intervals are indicated as error bars .

Determination of the critical point

The phase boundary between WSM and DM is determined by an onset of finite DOS at $E = 0$ and also by an onset of finite averaged velocity of the Weyl cone. The DOS at $E = 0$ vanishes for smaller disorder strengths. It starts to take a finite value when W is greater than a critical disorder strength. To determine this critical disorder strength without ambiguity, we first select a set of data points in the $\rho(0) - W$ figure (typically five to eight data points), which are in the DM region within the finite-size-scaling error bar (explained above), but which are sufficiently close to the WSM region. We applied a W -

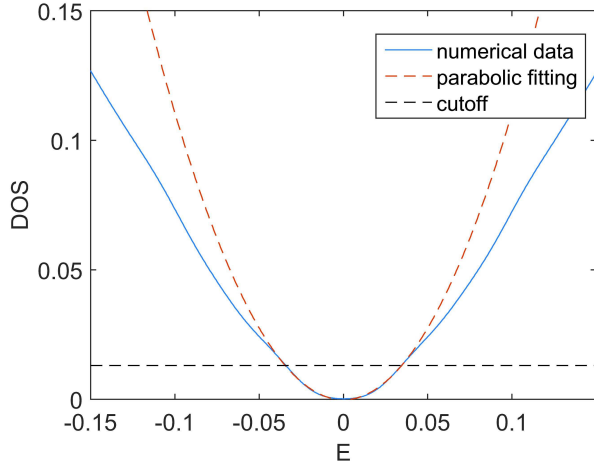


FIG. 12. (color online) A parabolic fitting of the DOS at $W = 1.5$ and $\beta = -0.6$. The blue solid line is from numerical data and the red dashed line is a E^2 -fitting curve. To exclude those data points away from $E = 0$, we introduce a cutoff for the DOS ($\rho < 0.013$), which is depicted by a black dashed horizontal line.

linear fitting for these data points, to regard the intercept of the fitting curve with the $\rho(0) = 0$ axis as the critical disorder strength W_c^{DM} (Fig. 13(a)).

On increasing the disorder strength in WSM phase, the inverse of the parabolic coefficient $1/b$ decreases continuously, only to converge to a small but non-zero constant value C_{res} in DM phase side. The small non-vanishing C_{res} is due to non-zero error bar stemming from the finite size scaling and the finite truncation of KPE. To derive a critical disorder strength as an onset disorder strength of finite averaged velocity, we regard this residual value C_{res} to be effectively zero and determine the critical strength from an intersect of a curve for $1/b$ as a function of W with $1/b = C_{res}$. To be more specific, we firstly fit out C_{res} from a set of those data points in the DM region which are close to the WSM region (data points encompassed by a grey dotted circle in Fig. 13(b)). We then collect another group of data points from the WSM region which are sufficiently close to the DM region (data points encompassed by an orange-colored dotted circle in Fig. 13(b)). As above, we applied a W -linear fitting for the latter group of the data points, and regard its intercept with $1/b = C_{res}$ as the critical disorder strength W_c^{WSM} (Fig. 13(b)).

Single parameter scaling

According to a scaling argument[26, 31], the density of states near the zero energy state follows scaling functions near the quantum critical point;

$$\rho(E) = \xi^{z-d} F(|E|\xi^z) = \delta^{(d-z)\nu} f(|E|\delta^{-z\nu}), \quad (18)$$

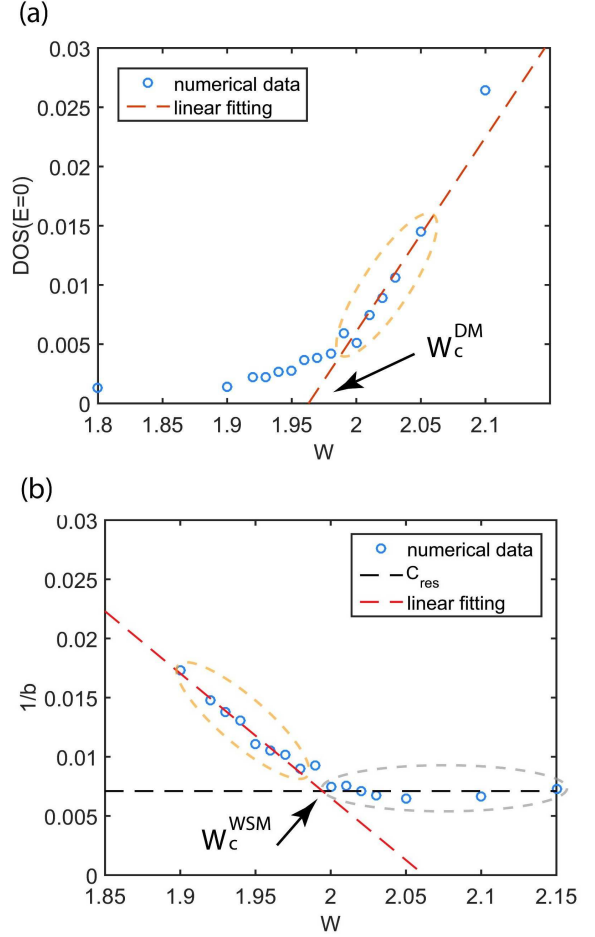


FIG. 13. (color online) (a) Determination of the critical disorder W_c^{DM} from the density of states (DOS) at $E = 0$. We selected a group of data points in the diffusive metal (DM) side and tried a linear fitting (red dashed line). The intercept with the $\rho(0) = 0$ axis is identified with the critical disorder strength W_c^{DM} . (b) Determination of the critical disorder W_c^{WSM} from the averaged velocity of the Weyl cone $1/b$. The data points in the DM side, which are near the WSM phase, take approximately small but constant value C_{res} (black dashed line). We applied a linear fitting to a group of data points in the WSM side (red dashed line). The intercept with $1/b = C_{res}$ is regarded as the critical disorder strength W_c^{WSM} , below which the averaged velocity starts to take a finite value.

where a characteristic length ξ scaled with the distance measured from the critical disorder strength, $\delta \equiv |W - W_c|/W_c$ with the critical exponent ν as $\xi \propto \delta^{-\nu}$. z denotes the dynamical exponent and the spatial dimension d is 3 in the present case. The critical disorder strength W_c is chosen to be the mean value between W_c^{WSM} and W_c^{DM} , since these two coincides with each other within the error bar. A scaling function $f(\dots)$ for the WSM phase and that for the DM phase are generally different from each other, while the critical exponents (ν and z) are universal. At the critical point, the δ -

dependences in Eq. (18) should cancel exactly, leading to $\rho(E) \propto \delta^{(d-z)\nu} (|E|\delta^{-z\nu})^{(d-z)/z} = |E|^{(d-z)/z}$. The calculated DOS at $W = W_c$ is nearly linear in $|E|$, suggesting that $z \simeq d/2$ [36, 37]. A comparison between the numerical data and the scaling form gives $z = 1.53 \pm 0.03$. In WSM phase, the DOS near $E = 0$ is scaled with $|E|^{d-1}$, so that the scaling form requires that its coefficient should be scaled with $\rho(E) \propto |E|^{d-1} \delta^{-d(z-1)\nu}$. Fitting of an coefficient of E^2 from Fig. 3b in the main text along this scaling form, i.e. $1/b \propto \delta^{-d(z-1)\nu}$, gives out $d(z-1)\nu = 1.24 \pm 0.06$. In DM phase, the DOS at $E = 0$ is scaled with $\rho(0) = \delta^{(d-z)\nu} f(0)$, along which the DOS at $E = 0$ from Fig. 3b in the main text is fitted, giving $(d-z)\nu = 1.47 \pm 0.06$. These two fittings in combination with $z = 1.53 \pm 0.03$ give us

$$\nu^{WSM} = 0.78 \pm 0.08, \quad (19)$$

$$\nu^{DM} = 1.00 \pm 0.13, \quad (20)$$

respectively. Though they do not coincide exactly, the discrepancy is at the same order of our estimated error bar, giving a weighted average ν as

$$\nu = 0.84 \pm 0.10. \quad (21)$$

In fact, with this critical exponent and $z = 1.53 \pm 0.03$ in hand, we can successfully fit all the data points of our DOS for $\rho(E) > \rho_c$ into two scaling functions, provided that ρ_c is chosen on the same order of error bars stemming from the finite size scaling (see above). As shown in a log-log plot of $\rho \delta^{-(d-z)\nu}$ versus $|E|\delta^{z\nu}$ (Fig. 14), all the data points collapse into two branches, where one branch (lower branch) corresponds to a scaling function for the WSM phase and the other (upper branch) to a scaling function for the DM phase respectively. With these results, we conclude that the critical nature of the WSM-DM phase transition in the unitary class follows the scaling law of Eq.(18) with $z = 1.53 \pm 0.03$ and $\nu = 0.84 \pm 0.1$.

Conductance and conductivity at $|\beta| = 0.55, 0.6$

The two-terminal conductance and conductivity for $|\beta| = 0.55$ and 0.6 are shown in Fig. 15. The conductance along the x direction (in-plane direction) are calculated for various system size ($L = 6, 8, 10, \dots, 30$), with periodic (G^p) or open boundary condition (G^o) in the y and z directions. We prepared 20 uncorrelated disorder realizations, over which the calculated conductance are averaged. The in-plane bulk conductivity σ_b is obtained from G^p by the linear fitting ($G^p = \sigma_b L + c$). We found that a finite bulk conductivity in the DM phase continuously reduces to zero toward the WSM-DM transition point. This behaviour is consistent with the self-consistent Born analyses [28] and a generalized Wegner's scaling relation [26, 34].

Note also that the two-terminal conductance in the WSM region for $|\beta| = 0.55$ and 0.6 strongly oscillate as

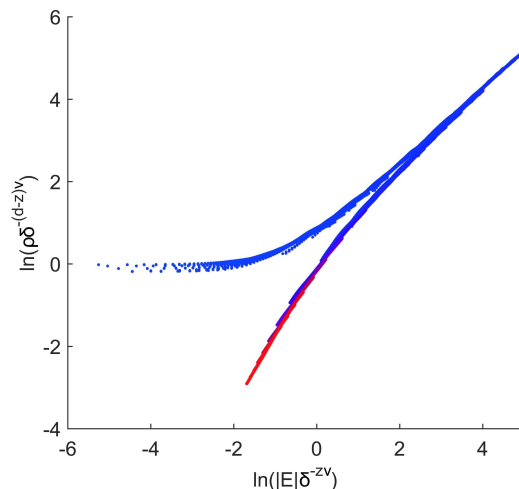


FIG. 14. (color online) A single parameter scaling of the density of states for $|\beta| = 0.6$ and W near the critical point with $\rho(E) > 0.02$. All the data points collapse onto two distinct branches which correspond to a scaling function for WSM phase (lower branch) and that for DM phase (upper branch), respectively.

a function of the cubic system size L , while the conductance in the WSM phase for $|\beta| = 0.45$ and 0.50 show much less prominent oscillation. The larger oscillations for $|\beta| = 0.55$ and 0.6 make it hard to determine the bulk conductivity in the WSM phase with smaller error bar (not shown in Fig. 15). The oscillation is due to (i) the very long mean-free path in the WSM phase and/or due to (ii) a mismatch between $\frac{2\pi N}{L}$ (N arbitrary integer less than L) and \bar{k}_0 (or \bar{k}_1) (the renormalized positions of the Weyl cones along the k_z axis).

* rshindou@pku.edu.cn

- [1] M. Z. Hasan and C. L. Kane, Rev. Mod. Phys. **82**, 3045 (2010).
- [2] Xiao-Liang Qi and Shou-Cheng Zhang, Rev. Mod. Phys. **83**, 1057 (2011).
- [3] K. v. Klitzing, G. Dorda, and M. Pepper, Phys. Rev. Lett. **45**, 494 (1980).
- [4] F. D. M. Haldane, Phys. Rev. Lett. **61**, 2015 (1988).
- [5] Xiao-Liang Qi and Taylor L. Hughes, and Shou-Cheng Zhang, Phys. Rev. B, **78**, 195424 (2008).
- [6] Cui-Zu Chang, et. al. Science **340** (2013).
- [7] Bodo Huckestein, Rev. Mod. Phys. **67**, 357 (1995).
- [8] Bernhard Kramer, Tomi Ohtsuki, and Stefan Kette- mann, Physics Reports **417**, 211 (2005).
- [9] M. Onoda and N. Nagaosa, Phys. Rev. Lett. **90** 206601 (2003).
- [10] B. I. Halperin, Phys. Rev. B **25** 2185 (1982).
- [11] E. Abrahams, P. W. Anderson, Licciardello L. C., and T. V. Ramakrishnan, Phys. Rev. Lett. **42** 673 (1979).
- [12] Tomi Ohtsuki, Bernhard Kramer, and Yoshiyuki Ono,

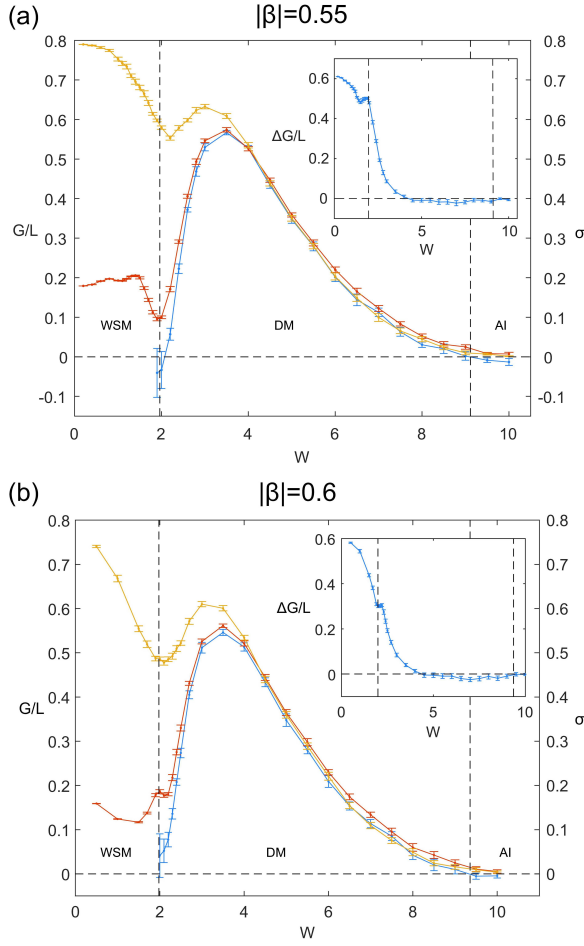


FIG. 15. (color online) In-plane (x -dir) bulk conductivity and conductance of the cubic system (L^3) at $|\beta| = 0.55$ (left) and 0.6 (right) as a function of the disorder strength W . Along the other two spatial directions (y and z -dir), we impose either periodic boundary condition G^p (red points with lines) or open boundary condition G^o (yellow points with lines) with $L = 30$. The bulk conductivity σ_b is obtained from the finite size scaling of the conductance with periodic boundary condition (blue points with line). The two vertical dotted lines (from left to right) stand for WSM-DM and DM-AI transition points respectively. The DM-AI transition point is determined by the localization length analysis, while the WSM-DM transition point is determined by the DOS analysis. (Inset) $\Delta G \equiv G^o - G^p$ for $|\beta| = 0.55$ (left) and 0.6 (right).

- Journal of the Physical Society of Japan **62**, 224 (1993).
- [13] J. T. Chalker and A. Dohmen, Phys. Rev. Lett. **75**, 4496 (1995).
- [14] A. A. Burkov and Leon Balents, Phys. Rev. Lett. **107**, 127205 (2011).
- [15] Kai-Yu Yang, Lu, Yuan-Ming, and Ying Ran, Physical Review B **84**, 075129 (2011).
- [16] R. Shindou and N. Nagaosa, Phys. Rev. Lett. **87**, 116801 (2001).
- [17] Ryo Okugawa and Shuichi Murakami, Phys. Rev. B **89**, 235315 (2014).
- [18] Keith Slevin and Tomi Ohtsuki, New Journal of Physics **16**, 015012 (2014).
- [19] Alexander Weiße, Gerhard Wellein, Andreas Alvermann, and Holger Fehske, Rev. Mod. Phys. **78**, 275 (2006).
- [20] See Supplemental Material.
- [21] A. MacKinnon and B. Kramer, Phys. Rev. Lett. **47**, 1546 (1981).
- [22] A. MacKinnon and B. Kramer, Zeitschrift fur Physik B Condensed Matter **53**, 113 (1983).
- [23] J L Pichard and G Sarma, Journal of Physics C: Solid State Physics **14**, L127 (1981).
- [24] Eduardo Fradkin, Phys. Rev. B **33**, 3263 (1986).
- [25] Ryuichi Shindou and Shuichi Murakami, Physical Review B **79**, 045321 (2009).
- [26] Koji Kobayashi, Tomi Ohtsuki, Ken-Ichiro Imura, and Igor F. Herbut, Phys. Rev. Lett. **112**, 016402 (2014).
- [27] H. Pixley, P. Goswami, and S. Das Sarma, arXiv:1502.07778 (2015).
- [28] Yuya Ominato and Mikito Koshino, Phys. Rev. B **89**, 054202 (2014).
- [29] Das Sarma S. and Hwang E. H. Phys. Rev. B **91**, 195104 (2015).
- [30] Pallab Goswami and Sudip Chakravarty, Phys. Rev. Lett. **107**, 196803 (2011).
- [31] S. V. Syzranov, V. Gurarie, and L. Radzihovsky, Phys. Rev. B **91**, 035133 (2015).
- [32] J.B. Pendry, A. MacKinnon, and P.J. Roberts, Proc. R. Soc. A **437**, 035133 (1992).
- [33] S. V. Syzranov, L. Radzihovsky, and V. Gurarie, Phys. Rev. Lett. **114**, 166601 (2015).
- [34] F.Wegner, Z. Phys. B **25**, 327 (1976).
- [35] Chui-Zhen Chen, Juntao Song, Hua Jiang, Qing feng Sun, Ziqiang Wang, and X. C. Xie, Phys. Rev. Lett. **115**, 246603 (2015).
- [36] H. Pixley, P. Goswami, and S. Das Sarma, arXiv:1505.07938 (2015).
- [37] S. V. Syzranov, P. M. Ostrovsky, V. Gurarie and L. Radzihovsky, arXiv:1512.04130 (2015).